Selective Disruption of Synaptic BMP Signaling by a Smad Mutation Adjacent to the Highly Conserved H2 Helix

Tho Huu Nguyen,* Tae Hee Han,* Stuart J. Newfeld,† and Mihaela Serpe*,[1]

*Section on Cellular Communication, *Eunice Kennedy Shiver* National Institute of Child Health and Human Development, National Institutes of Health, Bethesda, Maryland 20892 and †School of Life Sciences, Arizona State University, Tempe, Arizona 85287-4501

ORCID IDs: 0000-0003-1400-7978 (S.J.N.); 0000-0002-9205-8589 (M.S.)

ABSTRACT Bone morphogenetic proteins (BMPs) shape normal development and function via canonical and noncanonical signaling pathways. BMPs initiate canonical signaling by binding to transmembrane receptors that phosphorylate Smad proteins and induce their translocation into the nucleus and regulation of target genes. Phosphorylated Smads also accumulate at cellular junctions, but this noncanonical, local BMP signaling modality remains less defined. We have recently reported that phosphorylated Smad (pMad in *Drosophila*) accumulates at synaptic junctions in protein complexes with genetically distinct composition and regulation. Here, we examined a wide collection of *Drosophila Mad* alleles and searched for molecular features relevant to pMad accumulation at synaptic junctions. We found that strong *Mad* alleles generally disrupt both synaptic and nuclear pMad, whereas moderate *Mad* alleles have a wider range of phenotypes and can selectively impact different BMP signaling pathways. Interestingly, regulatory *Mad* mutations reveal that synaptic pMad appears to be more sensitive to a net reduction in Mad levels than nuclear pMad. Importantly, a previously uncharacterized allele, Mad^{8}, showed markedly reduced synaptic pMad but only moderately diminished nuclear pMad. The postsynaptic composition and electrophysiological properties of Mad^{8} neuromuscular junctions (NMJs) were also altered. Using biochemical approaches, we examined how a single point mutation in Mad^{8} could influence the Mad-receptor interface and identified a key motif, the H2 helix. Our study highlights the biological relevance of Smad-dependent, synaptic BMP signaling and uncovers a highly conserved structural feature of Smads, critical for normal development and function.

KEYWORDS BMP signaling; *Mad* alleles; *Drosophila* NMJ

BONE morphogenetic proteins (BMPs) modulate a wide variety of cellular processes via canonical and noncanonical signaling pathways (Massague 1990; Hogan 1996; Derynck and Zhang 2003). Misregulation of BMP signaling is associated with developmental abnormalities and disease states, highlighting the need for tight regulation of various BMP pathways. Like all members of the TGF-β superfamily, BMPs form biologically active dimers that initiate signaling by binding to a hetero-tetrameric complex of Ser/Thr kinases, known as Type I and Type II BMP receptors (BMPRs). Type II receptors are constitutive kinases that phosphorylate Type I receptors within a regulatory glycine-serine-rich (GS) domain to activate them. Activated Type I receptors bind to and phosphorylate the intracellular transducers of the BMP pathway, the R-Smads (Smad-1, -5 or -8 in vertebrates and Mad in *Drosophila*) (Feng and Derynck 2005; Schmierer and Hill 2007). Phosphorylated R-Smads (pSmads) have a propensity to trimerize that favors their dissociation from the receptors (Kawabata *et al.* 1998). In the canonical pathway, pSmads associate with co-Smads, translocate into the nucleus, and, in conjunction with other transcription factors, modulate expression of target genes. Activated BMPRs can also signal independently of Smads through noncanonical pathways that include mitogen-activated protein kinase (MAPK), LIM kinase, phosphatidylinositol 3-kinase/Akt (PI3K/Akt), and Rho-like small GTPases (Derynck and Zhang 2003; Moustakas and Heldin 2005; Zhang 2009). More recently, pSmad accumulation at cell membranes has been reported in at least two instances: (i) at tight junctions

Copyright © 2020 by the Genetics Society of America
doi: https://doi.org/10.1534/genetics.120.303484
Manuscript received August 27, 2019; accepted for publication July 16, 2020; published Early Online July 31, 2020.
Available freely online through the author-supported open access option.
[1]Corresponding author: *Eunice Kennedy Shriver* National Institute of Child Health and Human Development, National Institutes of Health, 35 Convent Dr., MSC 3762, Bldg. 35, Room 1C-1016, Bethesda, MD 20892. E-mail: mihaela.serpe@nih.gov

during neural tube closure (Eom *et al.* 2011), and (ii) at the *Drosophila* neuromuscular junction (NMJ) (Dudu *et al.* 2006; Smith *et al.* 2012). During neural tube closure, pSmad1/5/8 binds to apical polarity complexes and mediates stabilization of BMP/BMPR complexes at tight junctions (Eom *et al.* 2011); prolonged BMP blockade disrupts tight junctions and affects epithelial organization (Eom *et al.* 2012). In both cases, these Smad-dependent functions do not require transcriptional regulation. In epithelial cells, nuclear pSmad signals tend to be very strong, obscuring junctional pSmad signals. In contrast, at the fly NMJ, junctional pMad localizes at synaptic terminals [the contacts between motor neurons (MNs) and body-wall muscles], whereas nuclear pMad accumulates in MN nuclei. The spatial separation between nuclear and synaptic pMad was instrumental in the initial characterization of the Smad-dependent local BMP signaling pathway (Sulkowski *et al.* 2014, 2016).

Flies rely on BMP signaling for NMJ growth and neurotransmitter release (Marqués and Zhang 2006). Many of these functions are triggered by Gbb—a BMP7 homolog that binds to presynaptic BMPRII, Wishful thinking (Wit), and the BMPRIs, Thickveins (Tkv) and Saxophone (Sax). During canonical signaling, this high-order BMP/BMPR complex is endocytosed and retrogradely transported to the MN soma, where Mad is phosphorylated and regulates transcriptional programs with distinct roles in the development of the NMJ. Gbb and Wit also signal noncanonically through the effector protein LIM kinase 1 (LIMK1) to regulate synapse stability (Eaton and Davis 2005). A third BMP signaling modality, Smad-dependent synaptic BMP signaling, does not require Gbb but does require Wit, Tkv, Sax, and the postsynaptic type-A glutamate receptors (DiAntonio 2006; Sulkowski *et al.* 2014). We have previously demonstrated that synaptic pMad is involved in a positive feedback loop across the synaptic cleft. Active, postsynaptic type-A (GluRIIA-containing) glutamate receptors trigger presynaptic accumulation of pMad, which, in turn, functions to stabilize type-A receptors at postsynaptic densities (Sulkowski *et al.* 2014, 2016). Genetic and cell biology studies suggest that synaptic Mad is phosphorylated locally by activated BMPRs confined to the active zone, a region with massive (synaptic vesicles) exocytosis but no endocytosis. This region effectively traps BMPRs, precluding them from endocytosis and participation in canonical BMP signaling. But how does pMad, a product of an enzymatic reaction, remain associated with its own kinase?

To learn more about the structural features of Mad that may influence its association with the BMPRs, we have collected most of the existing *Drosophila Mad* alleles and compared them side-by side for the ability to sustain the two Smad-dependent signaling modalities: canonical BMP signaling, marked by pMad accumulation in MN nuclei, and synaptic BMP signaling, marked by pMad accumulation at synaptic terminals. Mad is a modular, highly conserved protein that contains an N-terminal MH1 (Mad homology 1) DNA binding domain, a C-terminal MH2 protein interaction domain, and a linker that has been implicated in the crosstalk with other signaling pathways (Hoodless *et al.* 1996). Changes in the structure and the oligomeric state of the MH2 domain contribute in two ways to the directionality of the signaling process (Wu *et al.* 2001). First, the MH2 mediates Mad binding to BMPRI and thus phosphorylation of its C-terminal SSXS motif, the site of BMP-dependent phosphorylation (Hoodless *et al.* 1996; Macías-Silva *et al.* 1996; Zhang *et al.* 1996). Second, the MH2 is critical to formation of Smad trimers that dissociate from BMPRs (Kawabata *et al.* 1998). In particular, the L3 loop has been implicated in mutually exclusive interactions with the BMPRI and the phosphorylated C-terminal SSXS motif (Wu *et al.* 2001). Most molecular lesions in our *Mad* collection map to the MH2 domain, including in the L3 loop, making this allelic series particularly suitable for studies on Mad–Tkv interactions.

Within this comprehensive collection, we found that strong *Mad* alleles generally disrupt both synaptic and nuclear pMad accumulation, whereas moderate *Mad* alleles have a broader range of phenotypes and can differentially impact different BMP signaling modalities. In particular, Mad^{8} showed drastically reduced synaptic pMad levels, but only moderately diminished nuclear pMad. The postsynaptic composition and electrophysiological properties of Mad^{8} NMJs were likewise altered. Using biochemical assays and structural modeling, we have examined how point mutations such as S359L, present in Mad^{8}, could influence the Mad–Tkv interface. Our study identified a new molecular determinant for this Mad–Tkv interaction, the well-conserved H2 helix. Several genetic variants identified in human patients map to H2, underscoring the relevance of this motif for normal development and function.

Materials and Methods

Fly stocks

Drosophila stocks used in this study are as follows: w^{1118}, Mad^{1}, Mad^{2}, Mad^{3}, Mad^{4}, Mad^{5}, Mad^{6}, Mad^{7}, Mad^{8}, Mad^{9}, Mad^{10}, Mad^{11}, Mad^{12} (Sekelsky *et al.* 1995), Mad^{k00237} (here Mad^{237}) (Dworkin and Gibson 2006), $Mad^{KG005817}$ (Bellen *et al.* 2004), $Mad^{8\text{-}2}$ (Wiersdorff *et al.* 1996), *Df(2L)C28* (Raftery *et al.* 1995), and $twit^{MI06552}$ (Venken *et al.* 2011). The flies were reared at 25° on Jazz-Mix food (Fisher Scientific). To control for larval crowding, eight to ten females were crossed with five to seven males per vial and passed to fresh vials every 3 days.

Molecular constructs

Flag-Mad plasmid was previously described (Shimmi and O'Connor 2003). Flag-Mad8 was generated by PCR followed by Gibson assembly (NEB) and the S359L substitution was verified by sequencing. The following PCR primers were utilized:

Mad8-For: 5′-CCAGTACTCGTTCCTCGCCACTCGGAATTCGCG CCCGGTCACTCG;

Mad8-Rev: 5′-GCGGTATTTTGCACACGGTTAGCGGATGGAATC CGTGGTGG.

To generate the Tac–Tkv construct, Tac extracellular and transmembrane sequences (*Hin*dIII–*Eco*RI fragment) (Ren *et al.* 2003) were joined with the PCR amplified wild-type or activated Tkv cytoplasmic domain in the pIB/V5-His vector (ThermoFisher). The activated Tkv chimera (Tac–TkvA) had a single residue substitution Q199D at the end of the GS box (Wieser *et al.* 1995).

The following Tkv primers were utilized:

Tkv-For: 5′-GCGTCCTCCTCCTGAGTGGGCTCTGTTTCACC TACAAGCGACGCGAGAAGC;
Tkv-Rev: 5′-GGCTTACCTTCGAACCGCGGGCCCTCTAGACAAT CTTAATGGGCACATCG.

Immunohistochemistry

Larvae were dissected as described previously in ice-cooled Ca^{2+}-free HL-3 solution (Stewart *et al.* 1994; Budnik *et al.* 2006). The samples were fixed in either 4% formaldehyde (Polysciences) for 30 min or in Bouin's fixative (Bio-Rad) for 3 min and washed in phosphate-buffered saline (PBS) containing 0.5% Triton X-100. Primary antibodies from the Developmental Studies Hybridoma Bank were used at the following dilutions: mouse anti-GluRIIA (MH2B), 1:200; rat anti-Elav (7E8A10), 1:200. Other primary antibodies were as follows: rabbit anti-phosphorylated Mad (pMad), 1:500, (a gift from C. H. Heldin), rabbit anti-GluRIIC, 1:1000 (Ramos *et al.* 2015), Cy5-conjugated goat anti-horseradish peroxidase (HRP), 1:1000 (Jackson ImmunoResearch Laboratories, Inc.). Alexa Fluor 488-, Alexa Fluor 568-, and Alexa Fluor 647- conjugated secondary antibodies (Molecular Probes) were used at 1:400. Larval filets and brains were mounted in ProLong Gold (Invitrogen). Samples of different genotypes were processed simultaneously and imaged under identical confocal settings using laser scanning confocal microscopes (CarlZeiss LSM780).

Fluorescence intensity measurements

Maximum intensity projections were used for quantitative image analysis in Fiji. To measure pMad at the synaptic terminal, synapse surface area was calculated by creating a mask around the HRP signal that labels the neuronal membrane. For each sample, a threshold was applied manually to the HRP and pMad channels to remove irrelevant low intensity pixels outside the NMJ area. The mean puncta intensity was calculated as the total fluorescence intensity signal of the puncta divided by their area. All intensities were normalized to control values within an experimental set. The same method was used to quantify synaptic GluRIIA and GluRIIC levels. For nuclear pMad, MNs nuclei were labeled with anti-Elav, then thresholds were applied to the Elav and pMad signals as above. Mean puncta intensity was calculated as the total fluorescence intensity signal of the puncta divided by the area of the puncta. Bouton area was calculated by separating the HRP-positive regions of interest surrounding synaptic pMad immunoreactivities. The GluRIIC-positive puncta were counted with Imaris 9.5.1 (Bitplane) by first converting the confocal stacks into 3D reconstructed NMJs, then applying built-in spot detection algorithms. Briefly, the point of maximum intensity in each spot was defined as the center of GluRIIC puncta. The intensity threshold was adjusted to detect all GluRIIC-positive spots. False positive and false negative spots were inspected manually and corrected via the edit and select functions.

Student's *t*-test was performed using R software (version 3.6.2) to evaluate statistical significance. All graphs represent mean value of all animals of indicated genotypes ± SEM.

Cell-based assay

A cell-based assay for BMP signaling was described previously (Shimmi and O'Connor 2003; Serpe and O'Connor 2006). In brief, S2 cells were transfected with Flag-Mad or Flag-Mad8. At 3 days after transfection, cells were incubated with 1nM Dpp (R&D Systems) for 1 hr, and cell extracts were analyzed by Western blotting. The pMad levels were revealed with anti-phospho-Smad 1/5 (Ser463/465) 41D10 (Cell Signaling) 1:200 and anti-Tubulin (Invitrogen) 1:500, and quantified relative to the Flag signal detected with anti-Flag M2 (Sigma) at 1:2000 using IRDye secondary antibodies for simultaneous detection on an Odyssey Infrared Imaging System (Li-Cor Biosciences).

For immunocytochemistry experiments, eight-well chambers (Fisher Scientific) were coated with 0.1 mg/ml Concanavalin A (Sigma) for 1 hr at 25°, then with 1 ng/ml anti-Tac antibodies M-A251, (BioLegend) for 1 hr at 25°. Transiently transfected S2 cells were grown for 3 days before spreading on ConA/anti-Tac- coated chamber for 1 hr at 25°. The surface-attached cells were fixed in 4% formaldehyde (Polysciences) for 15 min, then stained for pMad (anti-phospho-Smad 1/5, 41D10, 1:200, Cell Signaling), and Flag (anti-Flag, M2, 1:500, Sigma). FITC-conjugated goat anti-phalloidin, 1:500 (Invitrogen), Alexa Fluor 568-, and Alexa Fluor 647- conjugated secondary antibodies (Molecular Probes) were used at 1:400. Cells were mounted in DAPI-containing Prolong Gold (Invitrogen).

Electrophysiology

Recordings were performed on muscle 6, segment A3 of third instar larvae as previously reported (Qin *et al.* 2005). Briefly, wandering third-instar larvae were dissected in ice-cold, calcium-free physiological HL-3 saline (Stewart *et al.* 1994) and immersed in HL-3 containing Ca^{2+} before being shifted to the recording chamber. The calcium-free HL-3 saline contains (in mM): 70 NaCl, 5 KCl, 20 $MgCl_2$, 10 HCO_3, 5 trehalose, 115 sucrose, 5 HEPES, pH adjusted to 7.2 at room temperature. The recording solution was HL-3 with 0.5 mM $CaCl_2$. Intracellular electrodes (borosilicate glass capillaries of 1 mm diameter) were filled with 3 M KCl and resistances ranged from 12 to 25 MΩ. Recordings were done at room temperature from muscle cells with an initial membrane

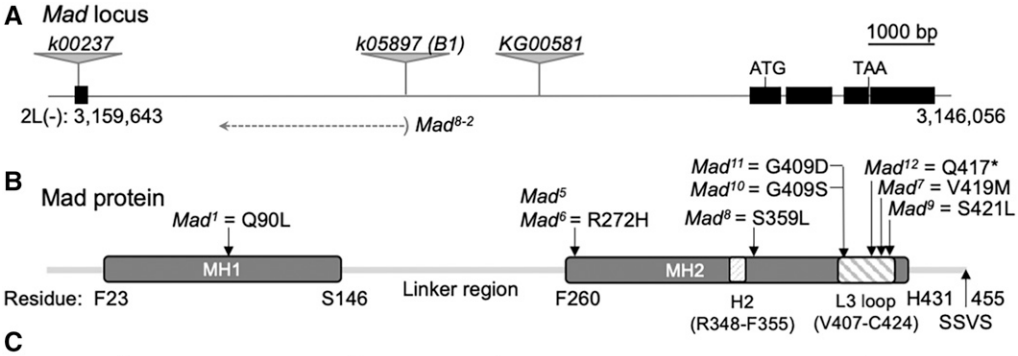

C

Allele	Mutation	Adults (% of expected)	Source/mutation citations	FlyBase ID
Mad^{1}	Q90L	0.0	(Sekelsky et al., 1995; Takaesu et al., 2005)	FBal0044913
Mad^{2}	nd	0.0	(Sekelsky et al., 1995)	FBal0044917
Mad^{3}	nd	0.0	(Sekelsky et al., 1995)	FBal0044918
Mad^{4}	nd	0.0	(Sekelsky et al., 1995)	FBal0044919
Mad^{5}	R272H	30.1	(Sekelsky et al., 1995; Takaesu et al., 2005)	FBal0044921
Mad^{6}	R272H	14.0	(Sekelsky et al., 1995; Takaesu et al., 2005)	FBal0044922
Mad^{7}	V419M	0.0	(Sekelsky et al., 1995; Takaesu et al., 2005)	FBal0044923
Mad^{8}	S359L*	0.0	(Sekelsky et al., 1995; Takaesu et al., 2005)	FBal0044924
Mad^{9}	S421L	3.0	(Sekelsky et al., 1995)	FBal0044925
Mad^{10}	G409S	0.0	(Sekelsky et al., 1995)	FBal0044914
Mad^{11}	G409D	7.3	(Sekelsky et al., 1995; Takaesu et al., 2005)	FBal0044915
Mad^{12}	Q417* (Stop)	0.0	(Sekelsky et al., 1995)	FBal0044916
Mad^{KG00581}	P insertion	0.0	(Bellen et al., 2004)	FBal0147791
Mad^{k00237}	P insertion	0.0	(Dworkin and Gibson, 2006)	FBal0064630
Mad$^{8-2}$	Imprecise excision of *B1*	0.0	(Wiersdorff et al., 1996)	FBal0052176

* S359 is an update to the numbering of S358 from Takaesu et al. 2005.

Figure 1 *Mad* alleles analyzed. (A) Diagram of the *Mad* locus and transposable element alleles. (B) Mad domain organization and point mutations. (C) List of *Mad* alleles analyzed with viability data.

potential between −50 and −70 mV, and input resistances of ≥ 4 MΩ. For miniature excitatory junction potentials (mEJC) recordings, the muscle cells were clamped to −80 mV. To calculate mean amplitudes and frequency of mEJCs, 100–150 events from each muscle were measured and averaged using the Mini Analysis program (Synaptosoft). Minis with a slow rise and falling time arising from neighboring electrically coupled muscle cells were excluded from analysis (Gho 1994; Zhang *et al.* 1998). To compare decay time constant of mEJCs between genotypes, 50 clear representative events from each recording were averaged and fitted using a double exponential equation of the form

$$I(t) = I_{fast}\ exp(-t/\tau_{fast}) + I_{slow}\ exp(-t/\tau_{slow}),$$

where I_x is the peak current amplitude of a decay component and τ_x is the corresponding decay time constant. To allow for easier comparison of decay times between genotypes weighted τ (ms) were calculated using the formula

$$\tau_w = (I_{fast}/(I_{fast} + I_{slow}))^*\tau_{fast} + (I_{slow}/(I_{fast} + I_{slow}))^*\tau_{slow}.$$

Electrical signals were recorded with an Axoclamp 2B amplifier (Axon Instruments). The signals were filtered at 1 kHz and digitized at 10 kHz by using an analog-digital converter (Digidata 1440A) and pCLAMP software (version 10.0, Axon Instruments). Data are presented as mean ± SEM. Two-tailed unpaired Student's *t*-test was used to assess statistically significant differences among genotypes. Differences were considered significant at $P < 0.05$.

Data availability

All reagents are available on request. The authors affirm that all data necessary for confirming the conclusions of the article are present within the article, main figures and tables.

Results

Analyses of pMad in larval MNs in distinct Mad alleles

To test the effect of *Mad* mutations on the distribution and levels of synaptic and nuclear pMad, 15 available *Mad* alleles were examined (Figure 1, A and B). Most of these alleles were isolated as dominant maternal enhancers of recessive *dpp* mutations (Raftery *et al.* 1995; Sekelsky *et al.* 1995; Chen *et al.* 1998). We crossed each of these alleles with *Df(2L)C28*, a small deficiency covering the *Mad* locus, counted the resulted progenies, and calculated the percent of expected adult progeny that were *trans*-heterozygous for the allele and the deletion (Figure 1C). As expected, we observed only a few *Mad*^{i}*/Df(2L)C28* adult escapers, with the largest escaper percentage from the weak *Mad*^{5} and *Mad*^{6} alleles, previously classified as hemizygous viable (Sekelsky *et al.* 1995). In all crosses, we observed larval and pupal lethality as *Mad*-deficient animals were unable to enter and/or complete metamorphosis. The *Mad*^{i}*/Df(2L)C28* larvae, henceforth referred to as "*Mad*^{i} mutants," have developmental delays and appear

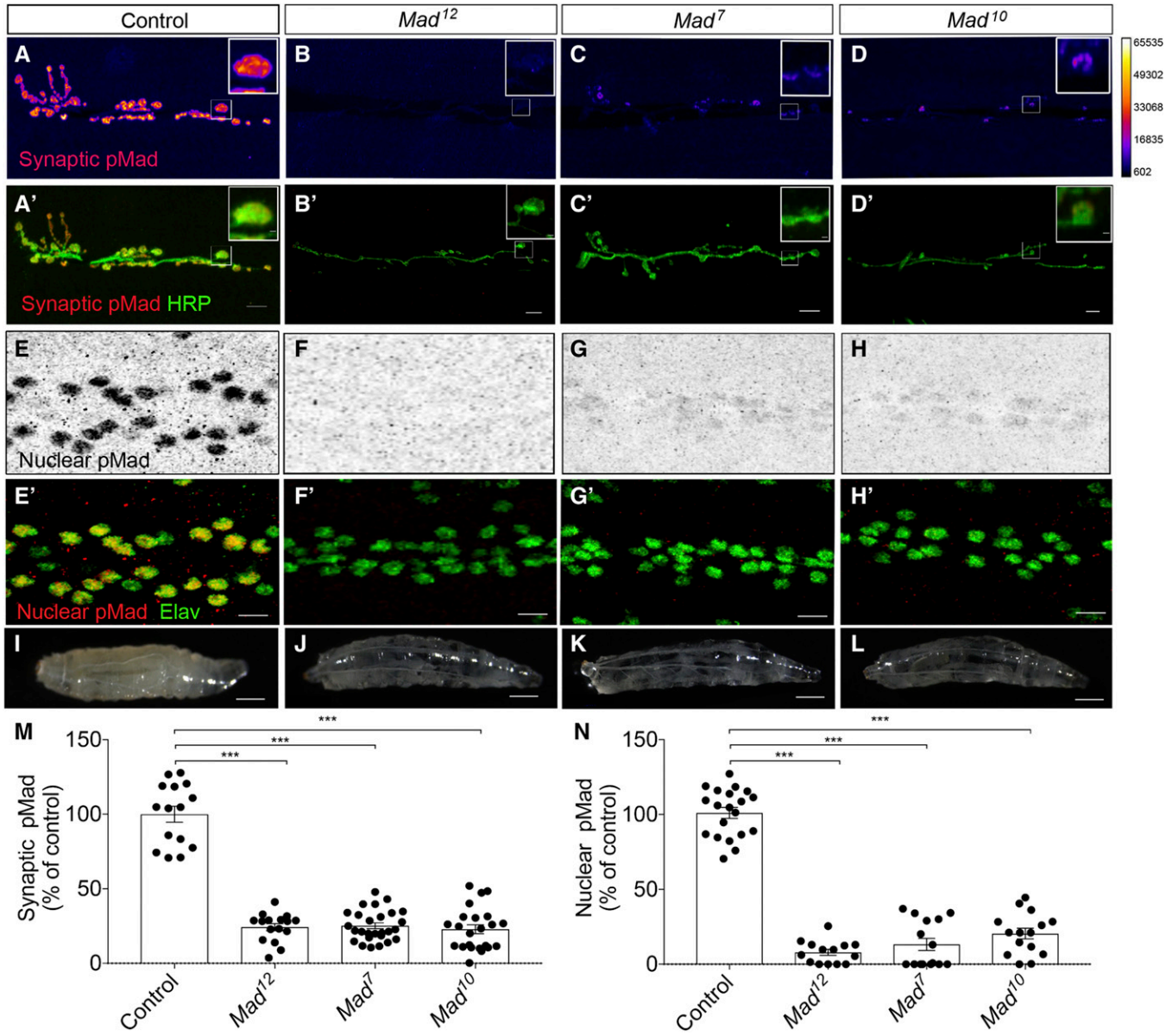

Figure 2 Strong *Mad* alleles disrupt both synaptic and nuclear pMad. (A–D) Representative confocal images of NMJ 6/7 boutons from third-instar larvae of indicated genotypes labeled for pMad (red) and HRP (green). Synaptic pMad is shown in Fire-lut representation in the upper panels; on the intensity scale, white represents peak intensity (~6000 arbitrary units, A.U.). (E–H) Confocal images of ventral nerve cord of larvae of indicated genotypes labeled with pMad (red in the merged panels) and Elav (green). In comparison with control animals (E), nuclear pMad is strongly reduced in Mad^{12} (F), Mad^{7} (G), and Mad^{10} (H) mutants. (I–L) Third instar control larvae (I) have an opaque appearance, while *Mad* mutants (J–L) are almost transparent due to severely reduced fat body. (M and N) Quantification of synaptic (M) and nuclear pMad (N) levels. See also Table 1. Bar, 10 μm (A–H) and 1 μm (details); 100 μm (I–L). Error bars indicate SEM. $***P < 0.0001$.

transparent due to reduced fat body. Since BMP signaling, primarily through Gbb/BMP7, is a central player in the energy homeostasis (Ballard *et al.* 2010), we used fat body accumulation as an additional metric for the severity of *Mad* mutant phenotypes (below).

To quantify the accumulation of pMad in MN nuclei, we costained third-instar larval ventral ganglia for pMad and Elav, a neuronal nuclear factor. For synaptic pMad, we quantified the pMad NMJ signals relative to anti-HRP, which labels neuronal membranes (Jan and Jan 1982). We used as a negative control the well-characterized Mad^{12} mutant to examine any residual pMad staining at the larval body wall muscle NMJ and in MNs (Figure 2, A and B). The protein encoded by Mad^{12} allele has a C-terminal truncation (Q417* stop) preceding the BMP-dependent phosphorylation site, $S^{451}SXS$, that abolishes any zygotic pMad signals (Sekelsky *et al.* 1995). Indeed, in Mad^{12} mutants, synaptic, and nuclear pMad were reduced by 80 ± 5% and 91 ± 5%, respectively (Table 1). The residual signals may be due to (i) maternal wild-type Mad protein that may persist at very low

Table 1 Summary of synaptic and nuclear pMad levels with the corresponding bouton area

		Synaptic pMad				Nuclear pMad				Bouton area			
Figure	Genotype	Mean	SEM	*P*	N	Mean	SEM	*P*	N	Mean	SEM	*P*	N
2	Control	100	2.47	1	30	100	2.08	1	29	100	2.08	1	16
2	Mad^{12}/Df	19.70	5.25	4.243E-11	18	9.36	5.19	<2.2E-16	17	22.37	3.73	1.82E-07	18
2	Mad^{7}/Df	23.55	4.44	1.698E-10	21	13.26	4.85	<2.2E-16	14	15.23	3.25	3.148E-08	14
2	Mad^{10}/Df	22.88	4.51	1.331E-11	23	20.49	3.60	<2.2E-16	15	19.54	1.05	4.878E-09	14
2	Mad^{4}/Df	24.07	1.51	<2.2E-16	17	7.82	2.33	<2.2E-16	12	8.63	2.17	1.595E-08	12
Additional data	Mad^{5}/Df	99.05	5.38	0.83	14	97.56	4.64	0.6252	17	97.67	4.71	0.8487	17
Additional data	Mad^{6}/Df	88.27	2.18	0.87	14	93.67	4.43	0.7717	13	84.73	5.61	0.1168	13
3	Mad^{237}/Df	63.99	3.01	1.585E-11	41	75.31	3.36	1.31E-06	19	59.30	3.65	4.766E-06	17
Additional data	Mad^{237}/Mad^{237}	58.58	3.02	1.47E-13	36	60.03	4.20	9.42E-09	17				
Additional data	Mad^{8-2}/Df	50.23	4.40	2.42E-11	21	57.35	4.11	3.1E-09	16	64.05	4.64	0.007	16
3	Mad^{9}/Df	62.92	4.43	1.516E-07	17	79.94	2.01	1.92E-05	16	65.34	4.38	0.0004	15
3	Mad^{11}/Df	61.75	1.48	1.398E-11	19	74.02	4.97	0.000199	13	68.79	4.33	0.001	15
4	Mad^{1}/Df	45.98	2.86	5.63E-10	19	31.62	5.06	1.02E-08	15	36.76	2.32	8.854E-08	18
	Mad^{2}/Df	N/A				N/A				N/A			
	Mad^{3}/Df	N/A				N/A				N/A			
	$Mad^{KG00581}/Df$	N/A				N/A				N/A			
5	Mad^{8}/Df	53.52	1.67	3.44E-09	22	75.42	3.26	1.42E-12	15	57.18	3.31	3.00E-07	26

levels during third-instar larval stages; (ii) cross reaction of the pMad antibodies with pSmox, the R-Smad of the Activin signaling pathway in *Drosophila*, that shares high homology with Mad over the C-terminus, or (iii) background staining.

Many *Mad* alleles have diminished HRP-labeled NMJ terminals and a significantly decreased bouton area, prompting us to find additional metrics to assess differences in staining at synaptic terminals. For example, in maximum intensity projections, the HRP-positive NMJ area in Mad^{12} mutants was reduced to 41.68 ± 6.15% ($n = 18, P < 0.0001$), compared to control ($n = 16$), whereas the bouton area, measured as HRP- and pMad-positive, was reduced to 22.37 ± 3.73% (Table 1 and *Materials and Methods*). For this study, we have selected the bouton area as the metric for NMJ growth. This parameter consolidates the number and size of synaptic boutons, and appears less prone to technical variability than the HRP-positive NMJ area. For consistency, we performed all NMJ analyses at NMJ 6/7 in the A3 abdominal segment.

Strong Mad alleles drastically reduce both synaptic and nuclear pMad signals

Mad^{7} and Mad^{10} are strong alleles with single residue substitutions within the MH2 domain: V419M in Mad^{7} and G409S in Mad^{10}, respectively (Sekelsky *et al.* 1995; Takaesu *et al.* 2005). Both residues map to the L3 loop of the MH2 domain, which has been implicated in mutually exclusive interactions with either BMPRIs or with the phosphorylated pS-X-pS tail of adjacent Smads in trimeric complexes (Wu *et al.* 2001). As expected, both Mad^{7} and Mad^{10} exhibited a drastic reduction of synaptic and nuclear pMad (Figure 2, C and D, quantified in M,N). Compared to the w^{1118} control, synaptic pMad levels were reduced to 24 ± 4% in Mad^{7} and to 23 ± 4% in Mad^{10}. Such levels were very close to those observed in the negative control, Mad^{12} (Figure 2B and Table 1). Nuclear pMad signals were similarly reduced to 13 ± 5% and 20 ± 5% in Mad^{7} and Mad^{10}, respectively. The Mad^{7}, Mad^{10}, and Mad^{12} mutant larvae appear translucent, with strongly reduced fat body, indicating severely impaired canonical BMP signaling (Figure 2, I–L).

Mad^{7}, Mad^{10}, and Mad^{12} were previously classified as null alleles based on their maternal effect enhancement of *dpp* (Sekelsky *et al.* 1995). Our analyses indicate that these alleles also behave as very strong hypomorphs during larval stages. In contrast, Mad^{4} was initially classified as a moderate allele; however, we found that both synaptic and nuclear pMad levels were drastically reduced in the Mad^{4} mutant larvae to 24 ± 2% and 8 ± 2% respectively, compared to control (Table 1). This result could not be explained by additional lesions on the Mad^{4} chromosome, because we analyzed $Mad^{4}/Df(2L)C28$ *trans*-heterozygous animals. Rather, we speculate that the unidentified molecular lesion in the Mad^{4} allele affects critical function(s) during larval development.

In contrast, the weak Mad^{5} and Mad^{6} mutants showed no significant changes in either synaptic or nuclear pMad levels during larval stages (Table 1) and had normal larval fat body (not shown). These alleles were isolated independently but have the same single residue change, R272H (Sekelsky *et al.* 1995; Takaesu *et al.* 2005). Nonetheless, these mutants yielded few adult escapers (Figure 1B), indicating that the substitution of this residue triggers critical deficits during later developmental stages.

Moderate Mad alleles exhibit differential effects on synaptic and nuclear pMad

While single point mutations disrupt functional domains within the Mad protein, the regulatory Mad^{237} allele (or Mad^{k00237}) has reduced overall Mad expression due to the insertion of a transposable element within the *5′UTR* of the *Mad mRNA* (Dworkin and Gibson 2006). Previous studies reported significant NMJ defects in Mad^{237} homozygous

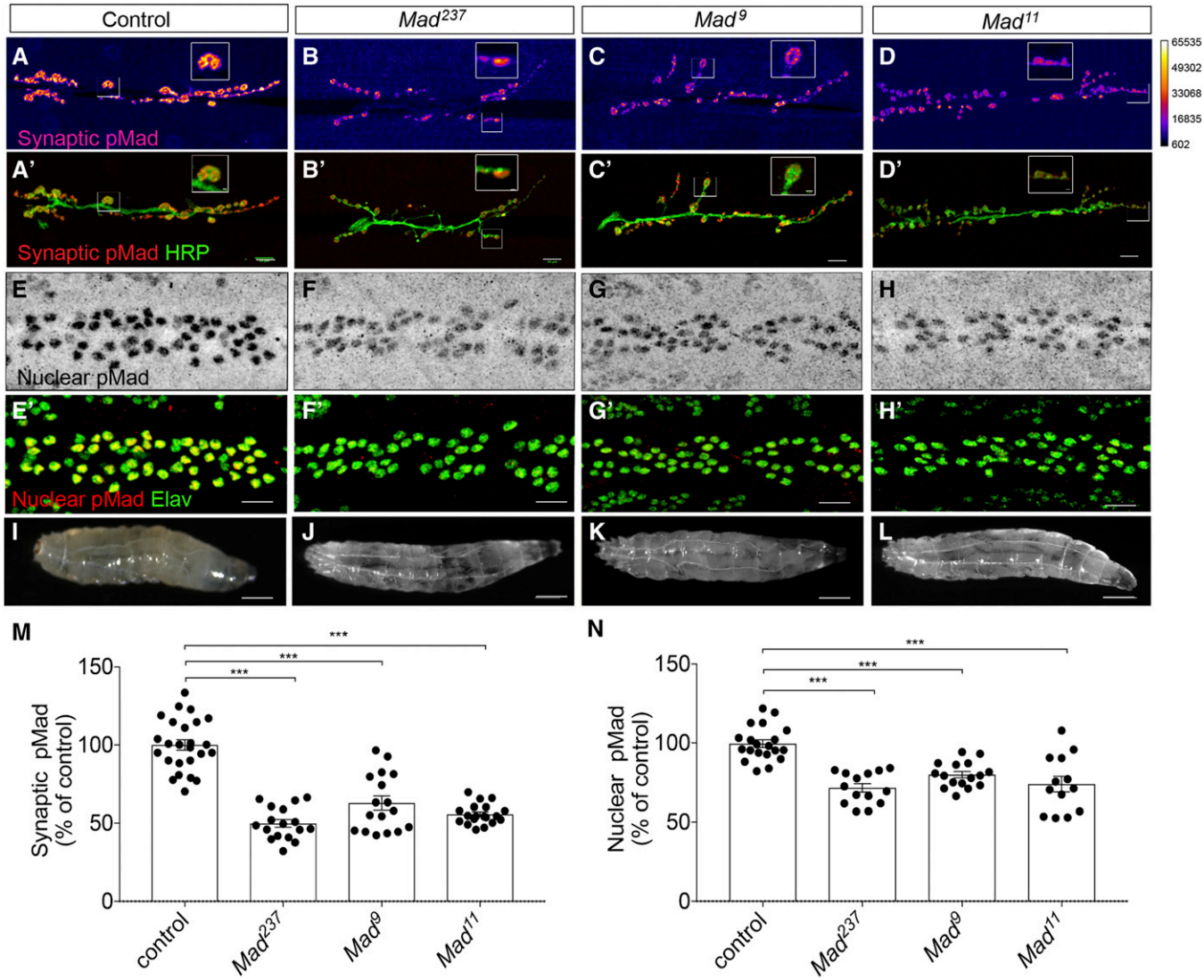

Figure 3 Moderate *Mad* alleles exhibit differential effects on synaptic and nuclear pMad. (A–H) Confocal images of NMJ 6/7 boutons and ventral nerve cord from third-instar larvae of indicated genotypes labeled for pMad (red) and HRP (green) (A–D) or Elav (green) (E–H). Synaptic pMad is showed in Fire-lut in the upper panels; on the intensity scale, white represents peak intensity (~6000 arbitrary units, A.U.). (E–H) Confocal images of ventral nerve cord of larvae of indicated genotypes labeled with pMad (red in the merged panels) and Elav (green). (I–L) Images of third instar larvae. *Mad* mutants (J–L) appear slightly translucent in comparison with control (I) due to mildly reduced fat body. (M and N) Quantification of synaptic (M) and nuclear pMad (N) levels. See also Table 1. Bar, 10 μm (A–H) and 1 μm (details); 100 μm (I–L). Error bars indicate SEM. ***$P < 0.0001$.

and *trans*-heterozygous combinations (Merino *et al.* 2009). We also found disruptions of pMad levels in Mad^{237} third-instar larvae (Figure 3, A and B and Table 1). Interestingly, the pMad levels were differentially disrupted in Mad^{237} mutants, with the synaptic pMad reduced to 64 ± 3% and the nuclear pMad to 75 ± 3% compared to control. A separate regulatory *Mad* allele, Mad^{8-2}, with a lesion in the first intron (Wiersdorff *et al.* 1996), showed a very similar phenotype (Table 1). Thus, synaptic pMad appears to be more sensitive to suboptimal Mad levels than nuclear pMad.

A similar trend was observed for two other moderate *Mad* alleles, Mad^{9}, and Mad^{11}, which code for single residue substitutions within the L3 loop of the MH2 domain (Sekelsky *et al.* 1995; Takaesu *et al.* 2005) (Figure 1). In these mutants, synaptic pMad was reduced to 63 ± 4% and 62 ± 4%, respectively, while nuclear pMad was reduced to 80 ± 4% and 74 ± 4% compared to control (Figure 3, C and D, quantified in M and N). A relatively small reduction in canonical BMP signaling was also evident when examining the larval fat body: these *Mad* mutants had modestly reduced fat body in comparison with the control (Figure 3, I–L). The greater reduction in synaptic pMad observed in moderate *Mad* alleles suggests that synaptic BMP signaling is sensitive to Mad net levels and to the integrity of the Mad-Type-I receptor interface, including the L3 loop.

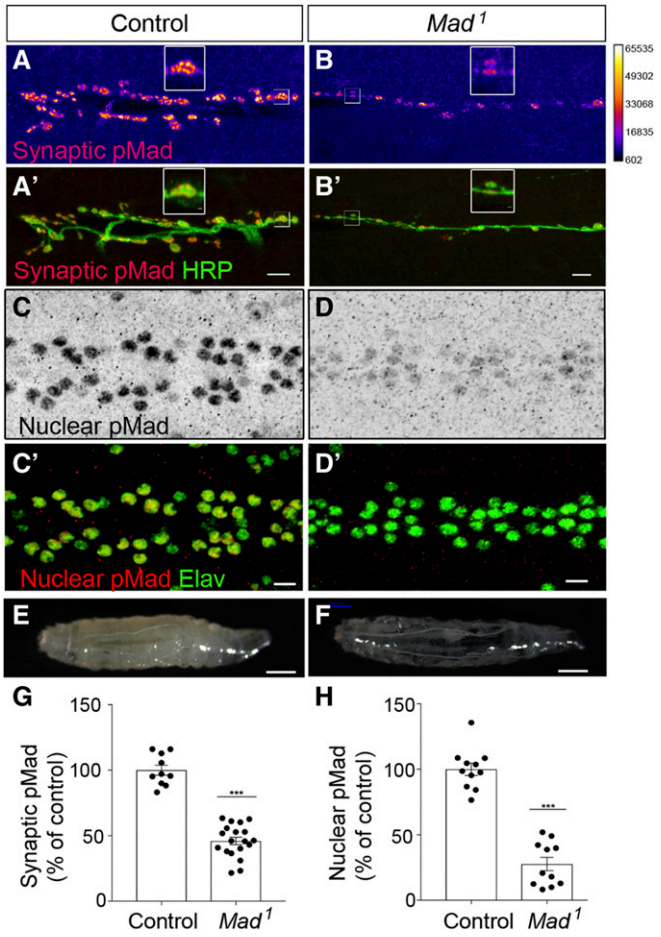

Figure 4 *Mad*^{1} is the only allele with a predominant effect on nuclear pMad. (A–D) Confocal images of third instar NMJ 6/7 boutons and ventral nerve cord from control and *Mad*^{1} mutants labeled for pMad (red) and HRP (green) (A and B) or Elav (green) (C and D). (E and F) The level of fat body is strongly reduced in *Mad*^{1} mutants (F) in comparison to control (E). pMad is shown in Fire-lut in the upper panels (A and B) and is quantified in (G–H). Bar, 10 μm (A–D) and 1 μm (details); 100 μm (E and F). Error bars indicate SEM. ***$P < 0.0001$.

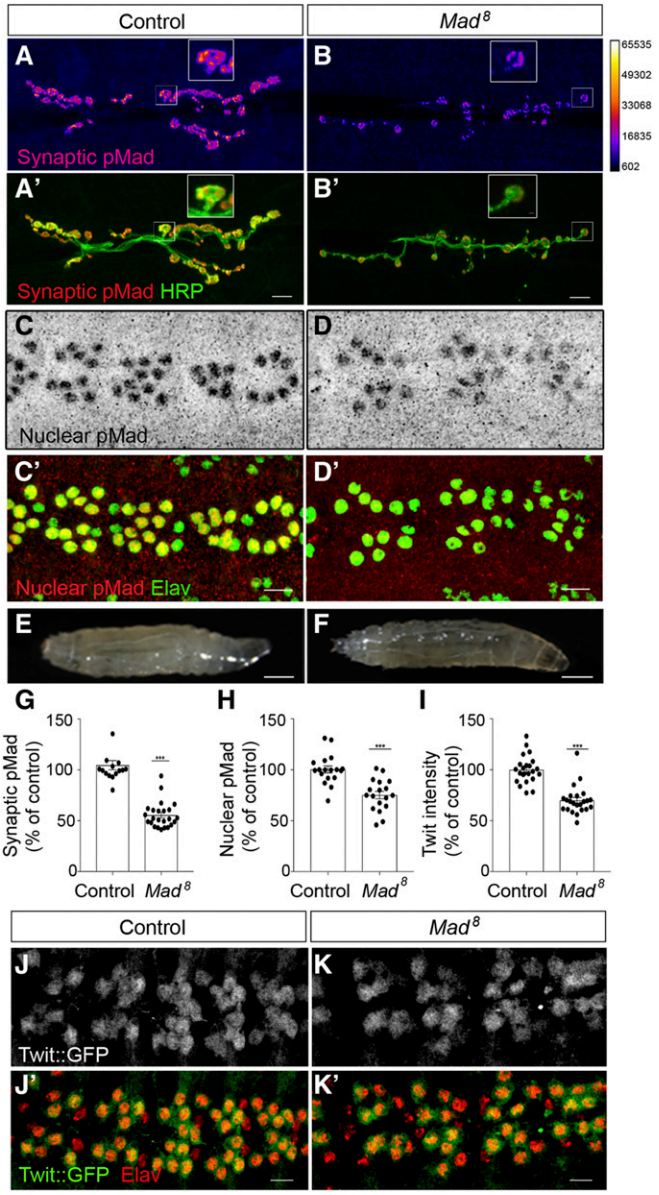

Figure 5 Disproportionate reduction of synaptic pMad in *Mad*^{8} mutants (A–D) Confocal images of NMJ 6/7 boutons and ventral ganglia in control and *Mad*^{8} third-instar larvae labeled for pMad (red) and HRP (green) (A and B) or Elav (green) (C and D). (E and F) Compared with control (E), fat body levels appear modestly reduced in *Mad*^{8} mutant larva (F). (G–I) Quantitative analysis of synaptic pMad (G), nuclear pMad (H) and Twit::GFP (I). (J and K) Confocal images of ventral nerve cord of indicated genotypes showing MN nuclei labeled with Twit::GFP (green) and Elav (red). Twit::GFP, a *MiMIC*-generated chimera, provides an additional readout for canonical BMP signaling. Genotypes: control (*Mi(MIC)twit*^{MI06552}/+), *Mad*^{8} (*Mad*^{8}/*Df(2L)C28*, *Mi(MIC)twit*^{MI06552}). Bar, 10 μm (A–D) and (J and K), 1 μm (details), 100 μm (E and F). Error bars indicate SEM. ***$P < 0.0001$.

Mad^{1} *is the only allele with a predominant effect on nuclear pMad*

Mad^{1} is the only known *Drosophila Mad* allele with a mutation in the DNA binding domain of Mad, (Q90L within the MH1) (Takaesu *et al.* 2005). *Mad*^{1} has been classified as a gain-of-function allele with dominant-negative activity because it exhibited an enhanced effect on *dpp*^{s6}/*dpp*^{hr4} vein phenotypes in comparison with a *Mad* deletion (Takaesu *et al.* 2005). Interestingly, *Mad*^{1} was one the few alleles in our study with relative reduction of nuclear pMad signals exceeding that of synaptic pMad: in *Mad*^{1} mutants, the pMad levels were reduced to 46 ± 3% and 32 ± 5% compared to control for synaptic and nuclear pMad, respectively (Figure 4, A–D). This likely reflects the molecular nature of this mutation that may disrupt Mad binding to DNA more than Mad interacting with other proteins. The fat body was also strongly reduced in *Mad*^{1} mutant, consistent with severe defects for canonical BMP signaling (Figure 4, E and F).

In our analyses, *Mad*^{2} and *Mad*^{3} alleles appeared more severe than the strong alleles noted above, *Mad*^{1}, *Mad*^{7}, *Mad*^{10}, and *Mad*^{12}. This is because *Mad*^{2} (or *Mad*^{3})/*Df(2L)*

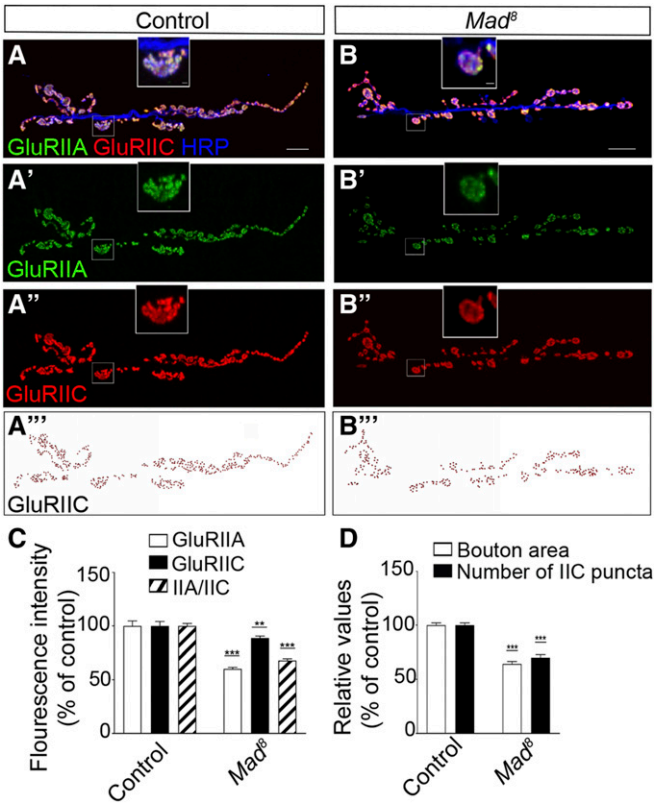

Figure 6 *Mad*^{8} mutants have altered postsynaptic iGluRs composition. (A and B) Confocal images of NMJ6/7 boutons from third instar larvae of control and *Mad*^{8} mutants labeled for HRP (blue), GluRIIA (green), and GluRIIC (red or black). The *Mad*^{8} NMJs show severe reduction of GluRIIA synaptic signals but modest decrease of GluRIIC levels (quantified in C). The bouton area and the number of synaptic contacts (GluRIIC-positive puncta) are similarly reduced in *Mad*^{8} mutants compared to control (quantified in D). Bar, 10 μm, 1 μm (details). Error bars indicate SEM. ***$P < 0.0001$; *$P < 0.05$; ns, $P > 0.05$.

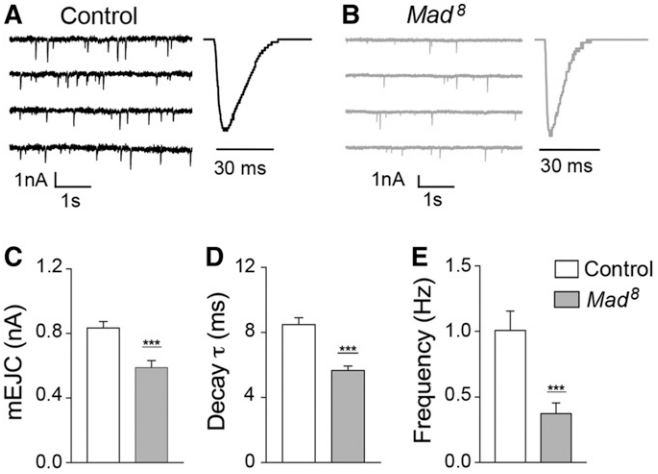

Figure 7 Electrophysiological deficits at *Mad*^{8} NMJs. (A and B) Representative traces of spontaneous junction currents (left) and average mEJC traces (right) recorded at 0.5 mM Ca^{2+} from muscle 6, segment A3, of control (A) and *Mad*^{8} NMJs (B). Summary graphs showing the mean amplitude (C), decay time constant (D) and mean frequency (E) of mEJCs. Error bars indicate SEM. ***$P < 0.0001$.

C28 animals died before reaching the third instar stage, whereas all other *Mad* mutants exhibited partial lethality as third-instar larvae. A similar result was obtained for *Mad*^{KG00581}, a strong allele generated by the insertion of a transposon within the *Mad* gene (Bellen *et al.* 2004). We did not characterize these strong *Mad* alleles further. Instead, in our search for molecular determinants relevant for pMad accumulation at synaptic junctions, we turned our attention to alleles that differentially modulate different BMP signaling pathways.

Mad^{8} *exhibits a disproportionate reduction of synaptic pMad*

Aside from *Mad*^{237} and the loop L3 mutants, most *Mad* alleles showed a relatively proportional reduction in both synaptic and nuclear pMad levels (Table 1). A notable exception was *Mad*^{8}, which codes for a protein with a single residue change, S359L, outside of any known functional motif (Takaesu *et al.* 2005). *Mad*^{8} exhibited a very significant reduction in synaptic pMad (to 54 ± 5% compared to control), but a more modest reduction in nuclear pMad (to 75 ± 5%) (Figure 5, A–D, Table 1). Moreover, there was a mild reduction of the fat body in *Mad*^{8} mutants in comparison to control third-instar larvae (Figure 5, E and F). We further confirmed the small effect of the *Mad*^{8} allele on nuclear pMad signals by examining MN expression of *twit (target of wit)*, a gene regulated by BMP signaling (Kim and Marques 2010). Using a *twit*::*GFP* insertion (Venken *et al.* 2011; Sulkowski *et al.* 2016), we found that Twit::GFP levels were reduced to 70 ± 4% in the *Mad*^{8} mutant MNs in comparison to the control (Figure 5, I–K). These data are consistent with a relatively moderate reduction of nuclear pMad in *Mad*^{8} larval MNs.

Since synaptic pMad mirrors the postsynaptic type-A glutamate receptors, we next examined the GluRIIA levels relative to total glutamate receptors, stained for GluRIIC, a subunit common for both type-A and type-B receptors (Marrus *et al.* 2004). GluRIIA levels were significantly reduced at *Mad*^{8} NMJs (to 67 ± 5% compared to control, $n = 30$) (Figure 6, A and B, quantified in 6C). In contrast, synaptic GluRIIC levels appeared only modestly diminished at *Mad*^{8} NMJs comparing to control (to 89 ± 6%, $n = 30$). This predominant GluRIIA reduction correlates with the disproportionate reduction of synaptic pMad at *Mad*^{8} NMJs.

To parse the effects of canonical and synaptic BMP signaling, we further examined bouton area and the number of glutamate receptor fields at *Mad*^{8} terminals (Table 1 and Figure 6A'''–B''', quantified in 6D). Both metrics were significantly reduced in *Mad*^{8} mutants, to 64 ± 4% of control for bouton area and to 70 ± 3% of control for the number of GluRIIC-positive puncta per NMJ. This follows very closely the observed reduction in canonical BMP signaling, as captured by diminished nuclear pMad and Twit reporter

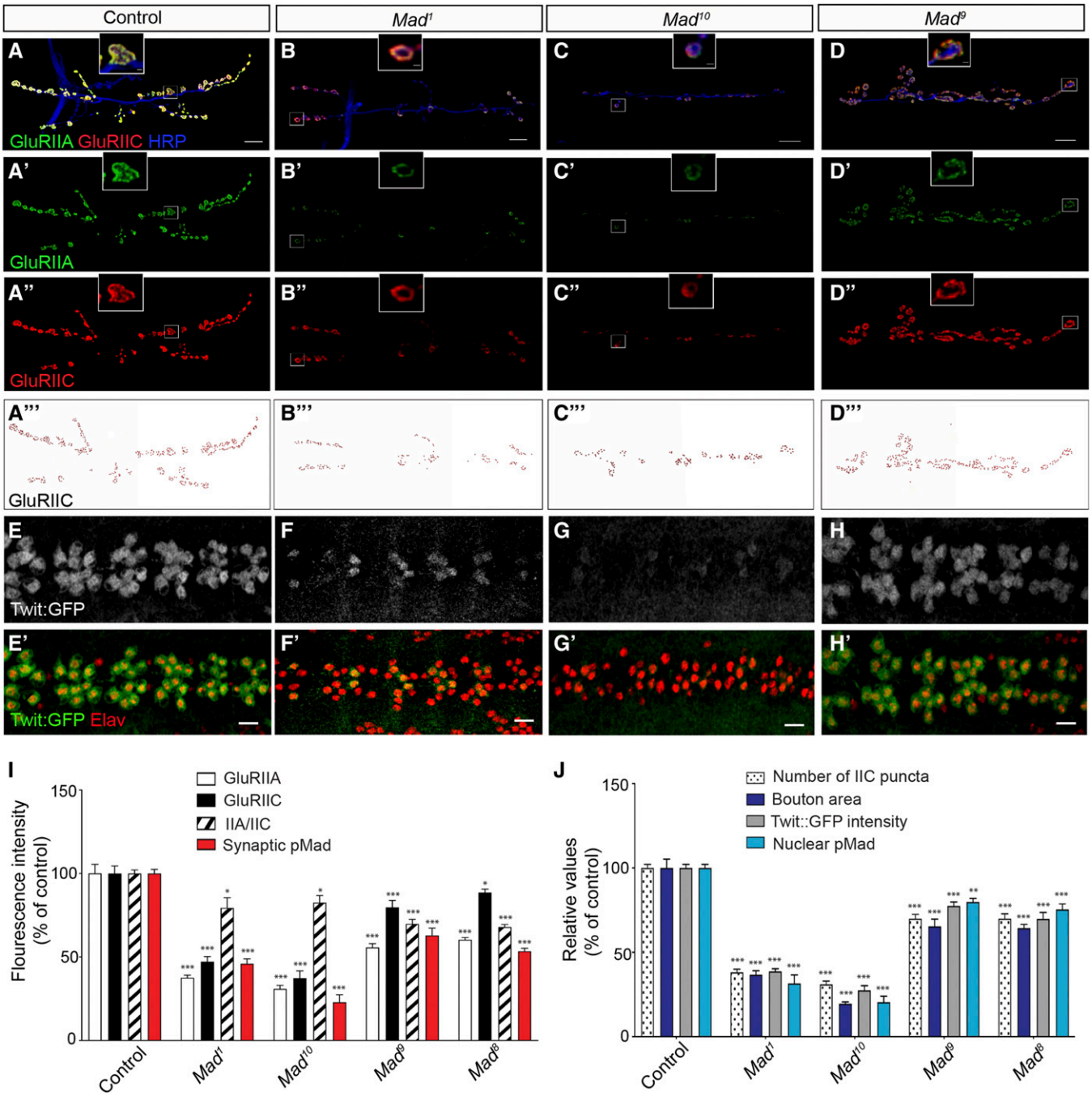

Figure 8 Synaptic and nuclear pMad capture different NMJ phenotypes. (A–D) Confocal images of NMJ6/7 boutons from third-instar larvae of indicated genotypes labeled for HRP (blue), GluRIIA (green), and GluRIIC (red or black). (E–H) Confocal images of ventral nerve cord of indicated genotypes showing MN nuclei labeled with Twit::GFP (green) and Elav (red). (I) Quantification of GluRIIA and GluRIIC synaptic signals for the indicated *Mad* alleles and comparison with the synaptic pMad. The correspondence between synaptic pMad and GluRIIA signals is particularly evident in moderate Mad^{8} and Mad^{9} alleles. (J) Quantification of bouton area, number of synaptic contacts (GluRIIC-positive puncta), Twit::GFP and nuclear pMad signal intensity for the indicated *Mad* alleles. Note the tight correlation of these metrics in these *Mad* alleles. Bar, 10 μm, 1 μm (details). Error bars indicate SEM. $^{***}P < 0.0001$; ns, $P > 0.05$.

intensity (Figure 5). The slightly more severe reduction in bouton area is probably caused by technical differences, since the bouton area was measured in collapsed [two-dimensional (2D)] NMJ stacks and the GluRIIC puncta in three-dimensional (3D) reconstituted NMJs. Together, our data indicate that the Mad^{8} NMJ deficits include (i) ~30% reduction in synaptic contacts and bouton area, reflecting the reduction in the canonical BMP signaling, and (ii) > 45% reduction in the synaptic GluRIIA levels, mirroring the more profound disruption of synaptic pMad.

Table 2 Summary of GluRIIA and GluRIIC synaptic levels

	GluRIIA			GluRIIC			IIA/IIC			N
Genotype	Mean	SEM	*P*	Mean	SEM	*P*	Mean	SEM	*P*	
Control	100	5.31	1	100	4.50	1	100	2.09	1	19
Mad^{10}/Df	37.65	2.15	<2.2E-16	45.08	4.37	2.3E-12	83.51	4.24	0.023	15
Mad^{1}/Df	37.45	1.56	<2.2E-16	47.20	3.08	<2.2E-16	79.34	6.24	0.0487	26
Mad^{9}/Df	55.65	2.28	1.088E-11	79.71	4.09	6.194E-09	69.82	2.76	6.05E-09	15
Mad^{8}/Df	60.21	1.38	2.775E-08	88.72	1.91	0.0002	67.87	1.64	1.756E-11	30

Electrophysiology recordings confirm strong deficits of local BMP signaling at Mad^{8} NMJs

GluRIIA-containing (type-A) receptors are determinants of the quantal size (the postsynaptic response to the release of single presynaptic vesicles) (DiAntonio *et al.* 1999). The reduced GluRIIA/GluRIIC ratio at Mad^{8} NMJs predicts that this mutant will have diminished quantal size. We tested this prediction by recording spontaneous junction currents from muscle 6 of control and Mad^{8} mutant third-instar larvae. The mEJC amplitude was significantly reduced at Mad^{8} mutant NMJs (0.59 ± 0.03 nA in Mad^{8}, $n = 11$, *vs.* 0.84 ± 0.04 nA in control, $n = 11$, $P = 0.0003$) (Figure 7, A–C). Furthermore, the decay time constant was decreased in Mad^{8} mutants (5.7 ± 0.23 ms for Mad^{8} *vs.* 8.51 ± 0.40 ms for control, $P < 0.0001$), indicating a switch to faster desensitizing receptors at Mad^{8} NMJs (Figure 7D). Since type-B receptors desensitize much faster than type-A (DiAntonio *et al.* 1999), these data are consistent with the reduced relative levels of type-A receptors (reduced GluRIIA/GluRIIC ratio) observed at these synapses (Figure 6). In addition, the mEJC frequency was significantly reduced in Mad^{8} mutants (0.38 ± 0.08 Hz in Mad^{8} *vs.* 1.01 ± 0.14 Hz in control; $P = 0.001$) (Figure 7E). The reduction in mEJC frequency could result from defects in the presynaptic release probability and the number and density of postsynaptic glutamate receptors consistent with the observed reduction in the number of postsynaptic receptors at Mad^{8} NMJs. Also, Twit, a target of canonical BMP signaling, has been implicated in presynaptic neurotransmitter release (Kim and Marques 2012). Together, our data suggest that Mad^{8} electrophysiological deficits represent a compound phenotype that includes (i) canonical BMP signaling deficits, such as reduced postsynaptic receptors and impaired neurotransmitter release, and (ii) synaptic BMP signaling defects, such as a disproportionate loss of GluRIIA-containing receptors.

Synaptic and nuclear pMad capture different NMJ phenotypes

To test whether the reduction of synaptic pMad at Mad^{8} NMJs reflects the unique molecular nature of this mutation or is an enhanced version of a common feature in other *Mad* alleles, we have expanded our in-depth analysis to include (i) Mad^{1}, the allele with a predominant effect on nuclear pMad; (ii) Mad^{10}, a strong *Mad* allele; and (iii) Mad^{9}, a moderate allele with a mutation in the L3 loop (Figure 1). We examined the synaptic levels of GluRIIA and GluRIIC, the IIA/IIC ratio, bouton area, the number of synaptic contacts (GluRIIC-positive puncta) per NMJ, and the Twit::GFP levels; and compared these results to control and Mad^{8} measurements (Tables 1, 2 and 3 and below).

We found that the strong alleles, Mad^{1} and Mad^{10}, have faint GluRIIA and GluRIIC synaptic signals; and drastically reduced number of synaptic contacts (Figure 8, A–C, quantified in I and J). Interestingly, both GluRIIA and GluRIIC immunoreactivities were similarly reduced at Mad^{1} and Mad^{10} NMJs, to 37% and 47% in Mad^{1} and 31% and 37% in Mad^{10} compared to control. Consequently, the IIA/IIC ratios were diminished by only ~20%, (Mad^{1}, to 79 ± 6% of control, $n = 26$; Mad^{10}, to 83 ± 4%, $n = 13$). In contrast, at Mad^{9} NMJs, the GluRIIA levels were reduced to 56 ± 2%, while the GluRIIC signals remained relatively robust (at 80 ± 4% of control). This unequal reduction of GluRIIA diminished the IIA/IIC ratio to 70 ± 3%, a value comparable to that observed for Mad^{8} (68 ± 2%, compare Figures 6D and 8D, quantified in 8I).

This analysis also showed that strong Mad alleles such as Mad^{1} and Mad^{10} have diminished bouton area and drastically reduced GluRIIC-positive puncta per NMJ, a direct consequence of their decreased nuclear pMad (Figure 8J and Table 1). In our hands, Mad^{10} larvae were extremely frail and showed significant lethality, suggesting our measurements underestimate the severity of Mad^{10} phenotypes. The Twit::GFP levels were likewise reduced in Mad^{1} and Mad^{10} mutants and remained apparent only in selective MNs (Figure 8, F and G, quantified in 8J). In contrast, Mad^{9} showed more robust NMJ growth, as illustrated by bouton area, the number of synaptic contacts, and modestly reduced Twit::GFP levels (Figure 8, H and J).

Notably, for each of the *Mad* alleles examined in detail, the metrics describing canonical BMP signaling (nuclear pMad and Twit::GFP levels, bouton area, and the number of synapses per NMJ) changed in synchrony, in tight correlation with each other (Figure 8J). This set of metrics therefore provides a good diagnostic for the status of canonical BMP signaling. In contrast, synaptic pMad segregates away from the canonical BMP signaling metrics and follows the GluRIIA levels instead. This is particularly evident for the moderate *Mad* alleles, Mad^{8} and Mad^{9}, which showed a more severe drop in GluRIIA levels than GluRIIC (Figure 8I). We suspect the

Table 3 Summary of Twit::GFP levels and the number of synaptic contacts (IIC puncta)

	Twit::GFP				GluRIIC puncta			
Genotype	Mean	SEM	*P*	N	Mean	SEM	*P*	N
Control	100	2.08	1	29	100	2.08	1	19
Mad^{10}/*Df*	27.45	2.91	<2.2E-16	18	31.04	1.89	<2.2E-16	13
Mad^{1}/*Df*	38.69	1.52	1.602E-15	13	38.25	1.72	<2.2E-16	26
Mad^{9}/*Df*	77.49	2.48	9.144E-09	24	69.97	2.62	4.018E-12	15
Mad^{8}/*Df*	69.86	3.87	2.174E-09	23	69.99	2.94	1.84E-11	30
Mad^{237}/*Df*	71.48	2.56	4.921E-12	33				

same is true for strong *Mad* alleles, including *Mad*^{1} and *Mad*^{10}; however, these alleles had extremely low levels of both synaptic pMad and postsynaptic glutamate receptors, impairing our ability to compare and correlate synaptic pMad with GluRIIA levels. Taking into account the shrunken NMJ areas, we estimated that the net levels of synaptic pMad, over an entire synaptic terminal, dropped to 16.8% and 4.4%, and the GluRIIC levels to 13.9% and 8.1% in *Mad*^{1} and *Mad*^{10}, respectively, compared with controls.

We have previously shown that synaptic pMad accumulates at active zones in puncta juxtaposing the postsynaptic densities (Sulkowski *et al.* 2016). This distribution near the presynaptic membrane together with the short life-time of pMad prompted us to propose that synaptic pMad (i) is generated locally by active BMP/BMPR signaling complexes, and (ii) remains associated with its own kinase, the activated Type I BMPR Tkv, in complexes anchored at the active zone by *trans*-synaptic interactions. Such signaling complexes, comprised of ligands bound to tetrameric (Type I and II) BMPRs and pSmads, have also been observed at vertebrate cellular junctions (Eom *et al.* 2011). At the fly NMJ, Mad mutations that impact the Mad-BMPR interface should disrupt not only the binding and phosphorylation of Mad, but also the accumulation of pMad-BMPR complexes at synaptic sites. The *Mad*^{9} allele codes for a single residue substitution (S421L) in the L3 loop at the interface between Mad and Tkv. This mutant is predicted to (i) bind to Tkv suboptimally, which can account for its reduced nuclear pMad levels, and to (ii) dissociate faster, which can further diminish its synaptic pMad. Indeed, our analysis of *Mad*^{9} NMJs captures both phenomena. In addition, our comparison of multiple *Mad* alleles confirms that synaptic and nuclear pMad specify distinct NMJ features. In particular, the correlation between synaptic pMad and GluRIIA is consistent with our previous findings that synaptic pMad is part of a positive feedback loop that functions to stabilize GluRIIA-containing receptors at synaptic sites (Sulkowski *et al.* 2014, 2016).

Biochemical analyses reveal faster dissociation of Mad8-Tkv complexes

To understand how *Mad*^{8} can have disproportionate influence on synaptic pMad accumulation, we examined its phosphorylation levels using a tissue culture-based signaling assay (Serpe and O'Connor 2006). We transfected S2 insect cells with either wild-type or S359L Mad constructs and presented them with 0.1 nM Dpp, the fly ortholog of BMP2/4. Dpp triggered a robust increase in pMad levels compared with the nontreated control (Figure 9, A and B); however, pMad accumulation in cells transfected with Flag-Mad-S359L, called here Mad8, was only 50% when compared to control. This result could not be explained by a disruption of Mad levels; western blot analysis indicated similar levels of the internal control, the Flag epitope. Instead, the difference in pMad signals suggests that the S359L substitution impacts the ability of Mad8 to bind to, and/or be phosphorylated by, activated Tkv.

Since *Mad*^{8} predominantly disrupts synaptic pMad, we hypothesize that Mad8 also prematurely dissociates from BMP/BMPR signaling complexes at the cell membrane. To test this possibility, we generated a Tac–Tkv chimera, where the Tkv intracellular domain was fused with the N-terminal and transmembrane domain of human Tac, the low affinity IL-2 receptor alpha chain (Ren *et al.* 2003). We also generated a Tac-activated Tkv chimera, referred here as Tac–TkvA, by introducing the Q199D substitution at the end of the GS box of Tkv; this substitution induces activation of the Ser/Thr kinase domains within TGF-β Type I receptors (Wieser *et al.* 1995).

In the presence of Tac–Tkv, both Mad and Mad8 were detectable throughout cells, including at cell membranes (Figure 9B); however, no pMad immunoreactivity was visible, indicative of an inactive Ser/Thr kinase. In the presence of activated Tac–TkvA, cotransfection of Mad induced massive pMad accumulation throughout the cell. In contrast, cotransfection of Mad8 elicited only nuclear pMad accumulation. Quantification of the pMad levels showed a drastic reduction of nuclear pMad for Mad8 (to 50% compared to control, Mad transfected cells), and an even more profound reduction of pMad at cell membranes (to ~30% of control levels). Similar to signaling assays (Figure 9A), these reduced pMad levels could reflect (i) a disruption of the Tkv–Mad8 enzyme-substrate (E-S) interaction by reducing the E-S association (via reduced binding and/or increased dissociation) or increasing the energy of activation, or (ii) an incorrect, premature dissociation of the enzyme-product (E-P) complexes. Since pMad immunoreactivity at the cell membrane is diminished beyond the level in nuclei, the S359L substitution likely induces a faster dissociation of the Tkv-pMad8 (E-P) complexes. This interpretation is consistent with our *in vivo* findings that *Mad*^{8} mutants disproportionally affect pMad accumulation at synaptic terminals.

At this time, structures for Smad-Type I receptor complexes are not available, but site-directed mutagenesis and studies on related structures indicate that the L3 loops of R-Smads bind to the L45 loops of the receptors (Huse *et al.* 1999; Durocher *et al.* 2000) (Figure 9, C and D); residues on both L3 and L45 confer class-specificity during signaling, *i.e.*, BMP *vs.* Activin pathway. Also, the GS domain and N-terminal lobe of the receptor kinase appear to form an MH2 docking interface that positions the Smad SSXS C-tail adjacent to the catalytic pocket of the receptor kinase. An opposing concave

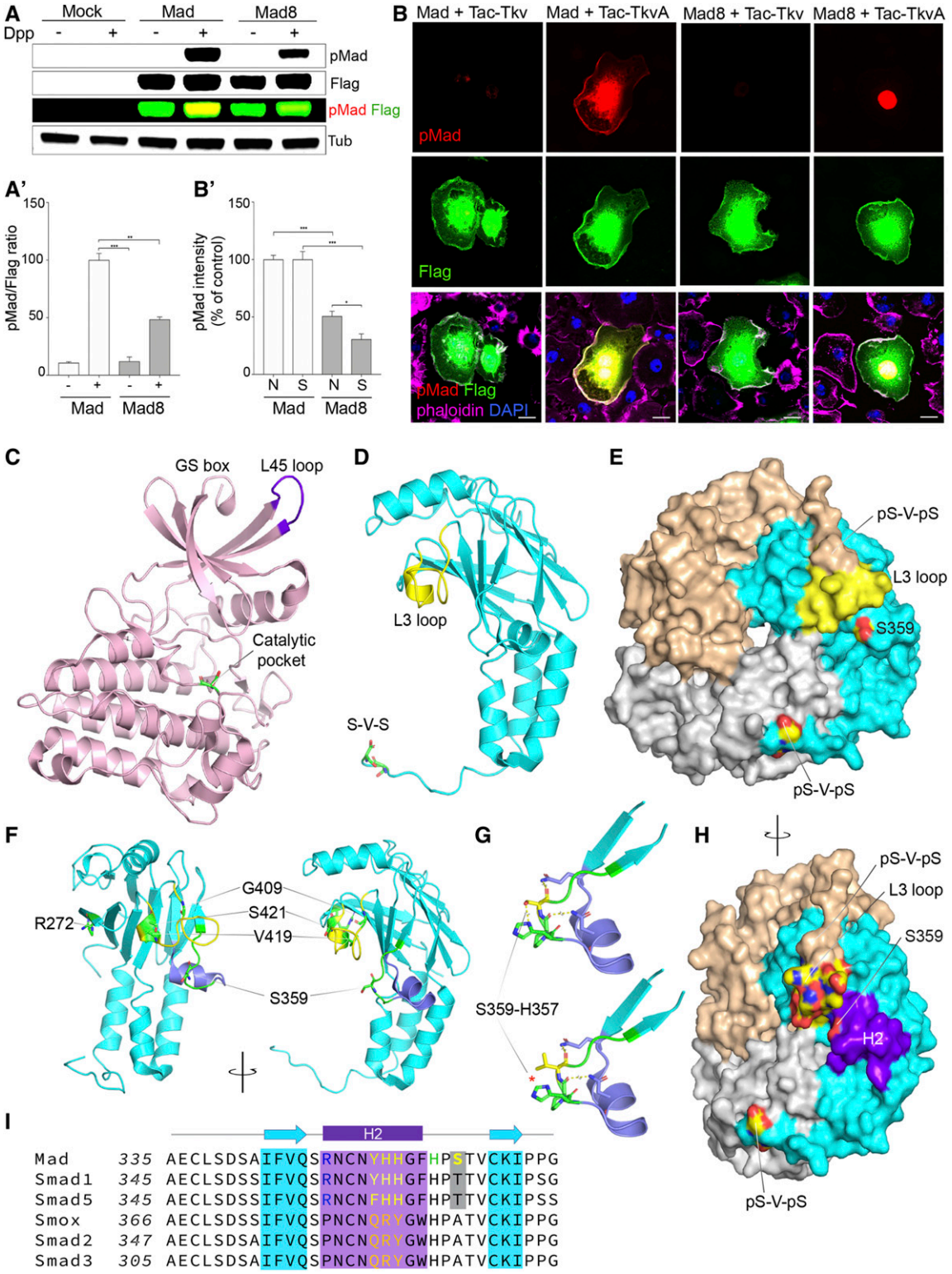

Figure 9 Biochemical analysis of Mad-Tkv interaction (A) Western blot analysis of whole extracts from S2 cells expressing Flag-Mad and Flag-Mad8 and treated with Dpp as indicated. Signaling is measured by the relative levels of pMad (red) and Flag (green) and is quantified in the histogram (A'). Compared to control, Mad8 has significantly reduced pMad levels upon Dpp exposure. (B) Confocal images of S2 cells transfected with Flag-Mad variants and Tac-Tkv chimeras as indicated, spread on anti-Tac coated surfaces and labeled for pMad (red), Flag (green), actin (phalloidin - magenta), and DNA (DAPI - blue). The activated Tac-TkvA chimera induces nuclear pMad accumulation when cotransfected with Flag-Mad, and, to a lesser extent, with Flag-Mad8, as quantified in (B'). pMad signals localize to cell surfaces only in Tac-TkvA/Flag-Mad cotransfected cells. (C) Structure of the Type I receptor (PDM code 3TZM). The L45 loop (magenta) interacts specifically with R-Smads. The N-lobe of the receptor, including the GS box and L45, forms a docking surface for MH2 and positions the S-V-S C-tail of Mad in the catalytic pocket. (D and E) Structure of the MH2 domain of *Drosophila* Mad (PDM

interface has been observed for all Smad MH2 domains, including the *Drosophila* Mad MH2. Once phosphorylated, pSmads have a high propensity to trimerize that favors their dissociation from receptors (Kawabata *et al.* 1998). Within a trimeric complex, the L3 loop engages the phosphorylated pS-X-pS tail of an adjacent Smad (Figure 9E). In addition, the L3 loop of R-Smads has been implicated in mutually exclusive interactions with the Type I receptors or with the phosphorylated pS-X-pS tail of other Smads in trimeric complexes (Wu *et al.* 2001). This model is also consistent with our experimental observations: Strong L3 mutations could effectively impair BMP signaling by disrupting both complexes, Mad-Tkv and Mad hetero-trimer complexes, while moderate alleles may cause more limited disruptions of Mad-Tkv interaction.

S359, the residue mutated in Mad8, maps within the same concave cavity of MH2 as the L3 loop and follows a highly conserved helix, H2 (Figure 9, F and I). Inspection of this region indicates that S359 stabilizes the highly conserved H357 via hydrogen bonds. Additional hydrogen bonds connect negative charges of the peptide backbone with N349 and Q346. Together these interactions appear to anchor and stabilize the H2 helix. Similar to L3, the H2 helix contains class-specific residues: Y^{352}HH in Smads of the BMP pathway, and QRY in the equivalent position in Smads of the Activin pathway (Figure 9I). The class-specific features of the H2 helix and its spatial orientation and proximity to the L3 loop suggest that H2 is critical for the Smad-Type I receptor interaction. In this scenario, the S359L substitution in Mad8 disrupts the Mad-Tkv interaction by (1) replacing a polar interface residue with a bulky hydrophobic one, (2) destroying the hydrogen bond S359-H357, and (3) likely shifting the position of H2, and the YHH class-specific residues, relative to the Mad-Tkv interface. This is consistent with our *in vivo* findings that the S359L substitution induces a predominant reduction of synaptic pMad.

Discussion

Our comprehensive analysis of numerous *Drosophila Mad* alleles revealed a rich phenotypic complexity for this important gene during different BMP signaling modalities and uncovered a new molecular determinant that confers class-specificity during TGF-β signal transduction.

Using the *Drosophila* NMJ system, we have quantified the effect of *Mad* alleles on both canonical and synaptic BMP signaling pathways. *Drosophila* requires canonical BMP signaling for NMJ growth. This pathway is triggered by muscle-derived BMPs that bind their receptors on MNs and form active BMP signaling complexes that are endocytosed and trafficked retrogradely to MN soma where they phosphorylate Mad (Marqués and Zhang 2006). pMad accumulation in MN nuclei quantitatively captures this canonical BMP response (Kim and Marques 2010). In addition, pMad accumulates at synaptic terminals as a result of a local, Smad-dependent BMP pathway that sculpts postsynaptic composition as a function of synapse activity (Sulkowski *et al.* 2014, 2016). We have previously shown that synaptic pMad is generated locally by BMP signaling complexes confined to the active zone, a region protected from endocytosis (Sulkowski *et al.* 2016). This suggests that MNs can monitor synapse status and then deploy BMP receptors to (i) the active zone, where they strengthen the synapse via local BMP signaling, or (ii) outside the active zone, where they engage in canonical signaling to expand the NMJ.

As expected, strong *Mad* alleles drastically reduce both nuclear and synaptic pMad levels (Figure 2 and Table 1). In contrast, moderate *Mad* alleles reveal differential requirements for different signaling modalities. First, uniform reduction of Mad levels preferentially reduced local pMad, indicating that pMad accumulation at synaptic junctions is more sensitive than pMad accumulation in MN nuclei (note Mad^{237} and $Mad^{8\text{-}2}$, Figure 3 and Table 1). This reduction may reflect (i) the distribution of Mad protein within the MNs, presumably more abundant in the soma than in neurites, or (ii) the nature of the Mad-BMPRs complexes, more transient in the soma but more stable at the synaptic junctions. Second, the prominent reduction of nuclear pMad in Mad^{1} mutants reinforces the idea that the MH1, the DNA binding domain of Mad affected in this mutant, is critical for nuclear accumulation of pMad and proper transcriptional control (Figure 4 and Table 1). Third, mutations in the L3 loop of the MH2 domain produced a set of moderate alleles (Mad^{9} and Mad^{11}) with predominant deficits in synaptic pMad, but also produced two of the strongest *Mad* alleles (Mad^{7} and Mad^{10}) (Figures 2 and 3). Since the L3 loop of R-Smads engages in a mutually exclusive interaction with the Type I receptors or with the phosphorylated C-tail of other Smads, we reason that strong L3 mutations may disrupt both sets of L3-mediated interactions, while moderate alleles may cause primarily Mad-Tkv dissociation. Finally, the disproportionate deficits of synaptic pMad in Mad^{8} revealed a role for the H2 helix in the modulation of the Mad-Tkv interaction. This highly conserved helix resides adjacent to the L3 loop and includes

code 3DIT) shown as monomer (D) and trimer (E). The L3 loop (yellow) is engaged in exclusive interactions with either the L45 loop of the receptor or the phosphorylated C-tail of another MH2 domain. (F) Map of MH2 Mad residues mutated in various *Mad* alleles. The two views of the structure are related by a 90° rotation around a vertical axis. (G) S359L in silico mutagenesis. S359 and its adjacent peptide backbone form hydrogen bonds with H357 and residues on the H2 helix (purple); the S359L substitution breaks the hydrogen bonds with H357 (red asterisk) and introduces a bulky moiety, shifting the H2. (H) Lateral view of the Mad MH2 trimer showing the close proximity of the H2 helix (purple) to the charged L3 surface (colored by atoms). (I) Alignment of R-Smad sequences indicating class specific residues in the H2 region, including the S359 (yellow). Bar, 10 μm (B). Error bars indicate SEM. $^{***}P < 0.0001$; $^{**}P < 0.001$; $^{*}P < 0.05$.

additional class-specific residues. These H2 features and its relative position to the MH2 concave cavity suggest that the H2 region is critical for the Smad-Type I receptor interaction. H2 maps outside the Smad trimer interface (Figure 7H), but it may further interfere with Smad-dependent transcription via Smad/cofactor interactions. Our *in vivo* findings favor a role for H2 in the modulation of Mad-Tkv interaction. The H2 contribution may be direct, by shaping the Mad-Tkv interface, or indirect, via recruiting other protein(s) that may stabilize Mad-Tkv complexes at cell junctions.

Indeed, other proteins appear to contribute to the stabilization of BMP signaling complexes at specialized cell junctions. Previous studies in the chick neural tube have shown that BMP signaling controls apicobasal polarity partly by enabling the pSmad1/5/8-dependent association of BMP signaling complexes with the PAR3-PAR5-aPKC complex at the tight junctions (Eom *et al.* 2011). Reduced Smad phosphorylation destabilizes the PAR complex and disrupts the tight junctions. In flies, loss-of-function disruptions of Bazooka(Par-3)-Par-6-aPKC complexes produced NMJs with significantly reduced number of boutons and increased levels of postsynaptic GluRIIA receptors (Ruiz-Canada *et al.* 2004). These phenotypes have been attributed to severe disruptions of microtubule stability, which may obscure a role for these complexes in modulation of BMP signaling.

In addition, posttranslational modifications of Mad and Tkv may strengthen or weaken their interaction and selectively modify nuclear and synaptic pMad. For example, Mad phosphorylation at S25 by Nemo (i) disrupts Mad association with Tkv at synaptic terminals, and (ii) favors nuclear export of pMad (Zeng *et al.* 2007; Merino *et al.* 2009). In both flies and mammals, posttranslational modifications such as ubiquitination limit receptor activity and trigger degradation or deactivation of both Smads and receptors, keeping these signaling components in check (Zhu *et al.* 1999; Dupont *et al.* 2009, Stinchfield *et al.* 2012). Interestingly, disruption of a number of components of the endocytic machinery elevate synaptic pMad and diminish nuclear pMad presumably by shifting receptor allocation from canonical BMP signaling to local, noncanonical signaling (O'Connor-Giles *et al.* 2008; Vanlandingham *et al.* 2013; Heo *et al.* 2017).

Misregulation of BMP signaling is associated with many developmental abnormalities and disease states. Our study indicates that the H2 helix region is critical to local BMP signaling and suggests that mutations in this region may disrupt specialized tight junctions throughout the animal kingdom. We searched for human genetic variants in the H2 region using the MARRVEL database (Model Organism Aggregated Resources for Rare Variant ExpLoration) (Wang *et al.* 2017). Interestingly, a Smad1 point mutation, Y362C that changes a class-specific residue within H2, was reported in the relative of a patient with colonic atresia, a congenital intestinal malformation that results in failure to pass meconium in newborns. Also, N361D substitution in Smad5 was found in a patient with malformation of the heart and great vessels. Finally, a N361-G365 deletion in Smad5 was reported in a patient with epileptic encephalopathy. While further studies are required to elucidate the functional impact of these genetic alterations on synaptic BMP signaling, these variants underscore the relevance of the H2 helix for normal development and function.

Acknowledgments

We thank Tom Brody and members of the Serpe laboratory for comments and discussions on this manuscript. We are grateful to C.H. Heldin for pMad antibodies. We also thank the Bloomington Stock Center at Indiana University for fly stocks and the Developmental Studies Hybridoma Bank at the University of Iowa for antibodies. T.H.N., T.H.H., and M.S. were supported by Intramural Program of the National Institutes of Health, *Eunice Kennedy Shriver* National Institute of Child Health and Human Development, grants ZIA HD008914 and ZIA HD008869 awarded to M.S. S.N. was supported by the National Institutes of Health (NIH) (OD024794).

Literature Cited

Ballard, S. L., J. Jarolimova, and K. A. Wharton, 2010 Gbb/BMP signaling is required to maintain energy homeostasis in Drosophila. Dev. Biol. 337: 375–385. https://doi.org/10.1016/j.ydbio.2009.11.011

Bellen, H. J., R. W. Levis, G. Liao, Y. He, J. W. Carlson *et al.*, 2004 The BDGP gene disruption project: single transposon insertions associated with 40% of Drosophila genes. Genetics 167: 761–781. https://doi.org/10.1534/genetics.104.026427

Budnik, V., M. Gorczyca, and A. Prokop, 2006 Selected methods for the anatomical study of Drosophila embryonic and larval neuromuscular junctions. Int. Rev. Neurobiol. 75: 323–365. https://doi.org/10.1016/S0074-7742(06)75015-2

Chen, Y., M. J. Riese, M. A. Killinger, and F. M. Hoffmann, 1998 A genetic screen for modifiers of Drosophila decapentaplegic signaling identifies mutations in punt, Mothers against dpp and the BMP-7 homologue, 60A. Development 125: 1759–1768.

Derynck, R., and Y. E. Zhang, 2003 Smad-dependent and Smad-independent pathways in TGF-beta family signalling. Nature 425: 577–584. https://doi.org/10.1038/nature02006

DiAntonio, A., 2006 Glutamate receptors at the Drosophila neuromuscular junction. Int. Rev. Neurobiol. 75: 165–179. https://doi.org/10.1016/S0074-7742(06)75008-5

DiAntonio, A., S. A. Petersen, M. Heckmann, and C. S. Goodman, 1999 Glutamate receptor expression regulates quantal size and quantal content at the Drosophila neuromuscular junction. J. Neurosci. 19: 3023–3032. https://doi.org/10.1523/JNEUROSCI.19-08-03023.1999

Dudu, V., T. Bittig, E. Entchev, A. Kicheva, F. Julicher *et al.*, 2006 Postsynaptic mad signaling at the Drosophila neuromuscular junction. Curr. Biol. 16: 625–635. https://doi.org/10.1016/j.cub.2006.02.061

Dupont, S., A. Mamidi, M. Cordenonsi, M. Montagner, L. Zacchigna *et al.*, 2009 FAM/USP9x, a deubiquitinating enzyme essential for TGFbeta signaling, controls Smad4 monoubiquitination. Cell 136: 123–135. https://doi.org/10.1016/j.cell.2008.10.051

Durocher, D., I. A. Taylor, D. Sarbassova, L. F. Haire, S. L. Westcott *et al.*, 2000 The molecular basis of FHA domain:phosphopeptide binding specificity and implications for phospho-dependent signaling mechanisms. Mol. Cell 6: 1169–1182. https://doi.org/10.1016/S1097-2765(00)00114-3

Dworkin, I., and G. Gibson, 2006 Epidermal growth factor receptor and transforming growth factor-beta signaling contributes to variation for wing shape in Drosophila melanogaster. Genetics 173: 1417–1431. https://doi.org/10.1534/genetics.105.053868

Eaton, B. A., and G. W. Davis, 2005 LIM Kinase1 controls synaptic stability downstream of the type II BMP receptor. Neuron 47: 695–708. https://doi.org/10.1016/j.neuron.2005.08.010

Eom, D. S., S. Amarnath, J. L. Fogel, and S. Agarwala, 2011 Bone morphogenetic proteins regulate neural tube closure by interacting with the apicobasal polarity pathway. Development 138: 3179–3188. https://doi.org/10.1242/dev.058602

Eom, D. S., S. Amarnath, J. L. Fogel, and S. Agarwala, 2012 Bone morphogenetic proteins regulate hinge point formation during neural tube closure by dynamic modulation of apicobasal polarity. Birth Defects Res. A Clin. Mol. Teratol. 94: 804–816. https://doi.org/10.1002/bdra.23052

Feng, X. H., and R. Derynck, 2005 Specificity and versatility in tgf-beta signaling through Smads. Annu. Rev. Cell Dev. Biol. 21: 659–693. https://doi.org/10.1146/annurev.cellbio.21.022404.142018

Gho, M., 1994 Voltage-clamp analysis of gap junctions between embryonic muscles in Drosophila. J. Physiol. 481: 371–383. https://doi.org/10.1113/jphysiol.1994.sp020446

Heo, K., M. Nahm, M. J. Lee, Y. E. Kim, C. S. Ki *et al.*, 2017 The Rap activator Gef26 regulates synaptic growth and neuronal survival via inhibition of BMP signaling. Mol. Brain 10: 62. https://doi.org/10.1186/s13041-017-0342-7

Hogan, B. L., 1996 Bone morphogenetic proteins in development. Curr. Opin. Genet. Dev. 6: 432–438. https://doi.org/10.1016/S0959-437X(96)80064-5

Hoodless, P. A., T. Haerry, S. Abdollah, M. Stapleton, M. B. O'Connor *et al.*, 1996 MADR1, a MAD-related protein that functions in BMP2 signaling pathways. Cell 85: 489–500. https://doi.org/10.1016/S0092-8674(00)81250-7

Huse, M., Y. G. Chen, J. Massague, and J. Kuriyan, 1999 Crystal structure of the cytoplasmic domain of the type I TGF beta receptor in complex with FKBP12. Cell 96: 425–436. https://doi.org/10.1016/S0092-8674(00)80555-3

Jan, L. Y., and Y. N. Jan, 1982 Antibodies to horseradish peroxidase as specific neuronal markers in Drosophila and in grasshopper embryos. Proc. Natl. Acad. Sci. USA 79: 2700–2704. https://doi.org/10.1073/pnas.79.8.2700

Kawabata, M., H. Inoue, A. Hanyu, T. Imamura, and K. Miyazono, 1998 Smad proteins exist as monomers in vivo and undergo homo- and hetero-oligomerization upon activation by serine/threonine kinase receptors. EMBO J. 17: 4056–4065. https://doi.org/10.1093/emboj/17.14.4056

Kim, N. C., and G. Marques, 2010 Identification of downstream targets of the bone morphogenetic protein pathway in the Drosophila nervous system. Dev. Dyn. 239: 2413–2425. https://doi.org/10.1002/dvdy.22368

Kim, N. C., and G. Marques, 2012 The Ly6 neurotoxin-like molecule target of wit regulates spontaneous neurotransmitter release at the developing neuromuscular junction in Drosophila. Dev. Neurobiol. 72: 1541–1558. https://doi.org/10.1002/dneu.22021

Macías-Silva, M., S. Abdollah, P. A. Hoodless, R. Pirone, L. Attisano *et al.*, 1996 MADR2 is a substrate of the TGFbeta receptor and its phosphorylation is required for nuclear accumulation and signaling. Cell 87: 1215–1224. https://doi.org/10.1016/S0092-8674(00)81817-6

Marqués, G., and B. Zhang, 2006 Retrograde signaling that regulates synaptic development and function at the Drosophila neuromuscular junction. Int. Rev. Neurobiol. 75: 267–285. https://doi.org/10.1016/S0074-7742(06)75012-7

Marrus, S. B., S. L. Portman, M. J. Allen, K. G. Moffat, and A. DiAntonio, 2004 Differential localization of glutamate receptor subunits at the Drosophila neuromuscular junction. J. Neurosci. 24: 1406–1415. https://doi.org/10.1523/JNEUROSCI.1575-03.2004

Massague, J., 1990 The transforming growth factor-beta family. Annu. Rev. Cell Biol. 6: 597–641. https://doi.org/10.1146/annurev.cb.06.110190.003121

Merino, C., J. Penney, M. Gonzalez, K. Tsurudome, M. Moujahidine *et al.*, 2009 Nemo kinase interacts with Mad to coordinate synaptic growth at the Drosophila neuromuscular junction. J. Cell Biol. 185: 713–725. https://doi.org/10.1083/jcb.200809127

Moustakas, A., and C. H. Heldin, 2005 Non-Smad TGF-beta signals. J. Cell Sci. 118: 3573–3584. https://doi.org/10.1242/jcs.02554

O'Connor-Giles, K. M., L. L. Ho, and B. Ganetzky, 2008 Nervous wreck interacts with thickveins and the endocytic machinery to attenuate retrograde BMP signaling during synaptic growth. Neuron 58: 507–518. https://doi.org/10.1016/j.neuron.2008.03.007

Qin, G., T. Schwarz, R. J. Kittel, A. Schmid, T. M. Rasse *et al.*, 2005 Four different subunits are essential for expressing the synaptic glutamate receptor at neuromuscular junctions of Drosophila. J. Neurosci. 25: 3209–3218. https://doi.org/10.1523/JNEUROSCI.4194-04.2005

Raftery, L. A., V. Twombly, K. Wharton, and W. M. Gelbart, 1995 Genetic screens to identify elements of the decapentaplegic signaling pathway in Drosophila. Genetics 139: 241–254.

Ramos, C. I., O. Igiesuorobo, Q. Wang, and M. Serpe, 2015 Neto-mediated intracellular interactions shape postsynaptic composition at the Drosophila neuromuscular junction. PLoS Genet. 11: e1005191. https://doi.org/10.1371/journal.pgen.1005191

Ren, Z., N. J. Riley, E. P. Garcia, J. M. Sanders, G. T. Swanson *et al.*, 2003 Multiple trafficking signals regulate kainate receptor KA2 subunit surface expression. J. Neurosci. 23: 6608–6616. https://doi.org/10.1523/JNEUROSCI.23-16-06608.2003

Ruiz-Canada, C., J. Ashley, S. Moeckel-Cole, E. Drier, J. Yin *et al.*, 2004 New synaptic bouton formation is disrupted by misregulation of microtubule stability in aPKC mutants. Neuron 42: 567–580. https://doi.org/10.1016/S0896-6273(04)00255-7

Schmierer, B., and C. S. Hill, 2007 TGFbeta-SMAD signal transduction: molecular specificity and functional flexibility. Nat. Rev. Mol. Cell Biol. 8: 970–982. https://doi.org/10.1038/nrm2297

Serpe, M., and M. B. O'Connor, 2006 The metalloprotease tolloid-related and its TGF-beta-like substrate Dawdle regulate *Drosophila* motoneuron axon guidance. Development 133: 4969–4979. https://doi.org/10.1242/dev.02711

Sekelsky, J. J., S. J. Newfeld, L. A. Raftery, E. H. Chartoff, and W. M. Gelbart, 1995 Genetic characterization and cloning of mothers against dpp, a gene required for decapentaplegic function in Drosophila melanogaster. Genetics 139: 1347–1358.

Shimmi, O., and M. B. O'Connor, 2003 Physical properties of Tld, Sog, Tsg and Dpp protein interactions are predicted to help create a sharp boundary in Bmp signals during dorsoventral patterning of the Drosophila embryo. Development 130: 4673–4682. https://doi.org/10.1242/dev.00684

Smith, R. B., J. B. Machamer, N. C. Kim, T. S. Hays, and G. Marques, 2012 Relay of retrograde synaptogenic signals through axonal transport of BMP receptors. J. Cell Sci. 125: 3752–3764. https://doi.org/10.1242/jcs.094292

Stewart, B. A., H. L. Atwood, J. J. Renger, J. Wang, and C. F. Wu, 1994 Improved stability of Drosophila larval neuromuscular preparations in haemolymph-like physiological solutions. J. Comp. Physiol. A Neuroethol. Sens. Neural Behav. Physiol. 175: 179–191. https://doi.org/10.1007/BF00215114

Stinchfield, M. J., N. T. Takaesu, J. C. Quijano, A. M. Castillo, N. Tiusanen *et al.*, 2012 Fat facets deubiquitylation of Medea/Smad4 modulates interpretation of a Dpp morphogen gradient. Development 139: 2721–2729. https://doi.org/10.1242/dev.077206

Sulkowski, M., Y. J. Kim, and M. Serpe, 2014 Postsynaptic glutamate receptors regulate local BMP signaling at the Drosophila neuromuscular junction. Development 141: 436–447. https://doi.org/10.1242/dev.097758

Sulkowski, M. J., T. H. Han, C. Ott, Q. Wang, E. M. Verheyen *et al.*, 2016 A novel, noncanonical BMP pathway modulates synapse maturation at the Drosophila neuromuscular junction. PLoS Genet. 12: e1005810 [corrigenda: PLoS Genet. 14: e1007343 (2018)]. https://doi.org/10.1371/journal.pgen.1005810

Takaesu, N. T., E. Herbig, D. Zhitomersky, M. B. O'Connor, and S. J. Newfeld, 2005 DNA-binding domain mutations in SMAD genes yield dominant-negative proteins or a neomorphic protein that can activate WG target genes in Drosophila. Development 132: 4883–4894. https://doi.org/10.1242/dev.02048

Vanlandingham, P. A., T. R. Fore, L. R. Chastain, S. M. Royer, H. Bao *et al.*, 2013 Epsin 1 promotes synaptic growth by enhancing BMP signal levels in motoneuron nuclei. PLoS One 8: e65997. https://doi.org/10.1371/journal.pone.0065997

Venken, K. J., K. L. Schulze, N. A. Haelterman, H. Pan, Y. He *et al.*, 2011 MiMIC: a highly versatile transposon insertion resource for engineering Drosophila melanogaster genes. Nat. Methods 8: 737–743. https://doi.org/10.1038/nmeth.1662

Wang, J., R. Al-Ouran, Y. Hu, S. Y. Kim, Y. W. Wan *et al.*, 2017 MARRVEL: integration of human and model organism genetic Resources to facilitate functional annotation of the human genome. Am. J. Hum. Genet. 100: 843–853. https://doi.org/10.1016/j.ajhg.2017.04.010

Wiersdorff, V., T. Lecuit, S. M. Cohen, and M. Mlodzik, 1996 Mad acts downstream of Dpp receptors, revealing a differential requirement for dpp signaling in initiation and propagation of morphogenesis in the Drosophila eye. Development 122: 2153–2162.

Wieser, R., J. L. Wrana, and J. Massague, 1995 GS domain mutations that constitutively activate T beta R-I, the downstream signaling component in the TGF-beta receptor complex. EMBO J. 14: 2199–2208. https://doi.org/10.1002/j.1460-2075.1995.tb07214.x

Wu, J. W., M. Hu, J. Chai, J. Seoane, M. Huse *et al.*, 2001 Crystal structure of a phosphorylated Smad2. Recognition of phosphoserine by the MH2 domain and insights on Smad function in TGF-beta signaling. Mol. Cell 8: 1277–1289. https://doi.org/10.1016/S1097-2765(01)00421-X

Zeng, Y. A., M. Rahnama, S. Wang, W. Sosu-Sedzorme, and E. M. Verheyen, 2007 Drosophila Nemo antagonizes BMP signaling by phosphorylation of Mad and inhibition of its nuclear accumulation. Development 134: 2061–2071. https://doi.org/10.1242/dev.02853

Zhang, Y. E., 2009 Non-Smad pathways in TGF-beta signaling. Cell Res. 19: 128–139. https://doi.org/10.1038/cr.2008.328

Zhang, Y., X. Feng, R. We, and R. Derynck, 1996 Receptor-associated Mad homologues synergize as effectors of the TGF-beta response. Nature 383: 168–172. https://doi.org/10.1038/383168a0

Zhang, B., Y. H. Koh, R. B. Beckstead, V. Budnik, B. Ganetzky *et al.*, 1998 Synaptic vesicle size and number are regulated by a clathrin adaptor protein required for endocytosis. Neuron 21: 1465–1475. https://doi.org/10.1016/S0896-6273(00)80664-9

Zhu, H., P. Kavsak, S. Abdollah, J. L. Wrana, and G. H. Thomsen, 1999 A SMAD ubiquitin ligase targets the BMP pathway and affects embryonic pattern formation. Nature 400: 687–693. https://doi.org/10.1038/23293

Communicating editor: D. Andrew